Relationship between H2 sorption properties and aqueous corrosion mechanisms in A2Ni7 hydride forming alloys (A = Y, Gd or Sm)

Véronique Charbonnier, Judith Monnier, Junxian Zhang, Valérie Paul-Boncour, Suzanne Joiret, Beatriz Puga, Lionel Goubault, Patrick Bernard, Michel Latroche

Relationship between H_2 sorption properties and aqueous corrosion mechanisms in A_2Ni_7 hydride forming alloys (A = Y, Gd or Sm)

Véronique CHARBONNIER[1], Judith MONNIER[1], Junxian ZHANG[1], Valérie PAUL-BONCOUR[1], Suzanne JOIRET[2], Beatriz PUGA[2], Lionel GOUBAULT[3], Patrick BERNARD[3] and Michel LATROCHE[1,*]

1. Université de Paris Est, ICMPE, CNRS-UPEC, UMR7182, 2-8 rue Henri Dunant, 94320 Thiais – France

2. CNRS, Sorbonne Universités – UPMC, UMR 8235, Laboratoire Interfaces et Systèmes Electrochimiques, 4 place Jussieu, 75005 Paris – France

3. SAFT, Direction de la Recherche, 111-113 Bd. Alfred Daney, 33074 Bordeaux – France

Abstract

Intermetallic compounds A_2B_7 (A = rare earth, B = transition metal) are of interest for Ni-MH batteries. Indeed they are able to absorb hydrogen reversibly and exhibit good specific capacity in electrochemical route. To understand the effect of rare earth on properties of interest such as thermodynamic, cycling stability and corrosion, we synthesized and studied three compounds: Y_2Ni_7, Gd_2Ni_7 and Sm_2Ni_7. Using Sieverts' method, we plot *pc*-isotherms up to 10 MPa and study hydride stability upon solid-gas cycling. Electrochemical cycling was also performed, as well as calendar and cycling corrosion study. Corrosion products were characterized by means of X-ray diffraction, electron diffraction, Raman micro-spectroscopy and scanning and transmission electron microscopies. Magnetic measurements were also performed to calculate corrosion rates. A corrosion mechanism, based on the nature of corrosion products, is proposed. By combining results from solid-gas cycling, electrochemical cycling and corrosion study, we attribute the loss in capacity either to corrosion or loss of crystallinity.

I. Introduction

In the late sixties, $LaNi_5$ was found to have the ability to absorb hydrogen reversibly. It resulted in a new type of secondary battery: Ni-MH battery [1]. Nowadays, AB_5 compounds (A: rare earth, B: transition metal) are still used as active material in negative electrodes for those batteries [2,3]. However, new AB_x alloys, with $2<x<5$, are intensively studied in order to enhance the specific capacity [4,5]. Those compounds are polymorphic, they crystallize either in $P6_3/mmc$ or $R\text{-}3m$ space groups. Their structures were first described by Khan [6]. They are composed of two different subunits: $[A_2B_4]$ and $[AB_5]$ [7]. On the one hand, AB_2 phases are known to absorb large amounts of hydrogen [8] but they undergo hydrogen-induced amorphization [9] especially for B=Ni; on the other hand, AB_5 phases have lower capacities, but better cycling stability. Consequently, using alloys composed of $[A_2B_4]$ and $[AB_5]$ subunits

* Corresponding author: michel.latroche@icmpe.cnrs.fr; +33 1 4978 1210; +33 1 4978 1203

is a good way to obtain alloys with both high capacity and good cycling stability. In the case of AB_3 phase, the $[A_2B_4]/[AB_5]$ ratio is high, so its cycling stability is rather low [10]. Therefore we choose to study a phase with a lower $[A_2B_4]/[AB_5]$ ratio, namely $AB_{3.5}$ (A_2B_7) phase.

A high weight specific capacity and a good cycling stability are really important for secondary batteries. It is well known that three different points can be involved in a poor electrochemical cycling [11]: the loss in electric contact due to decrepitation, amorphization and corrosion of active material.

In this paper, we study three different intermetallic compounds: Y_2Ni_7, Gd_2Ni_7 and Sm_2Ni_7. It has been demonstrated that the AB_2 phases are more stable for a R_A/R_B close to 1.225 [9,12]. For this reason we choose to use smaller rare earths. Moreover, yttrium has similar behavior as rare earths and has the benefit to be lighter; it should then lead to an increase in weight specific capacity. A systematic study of those three compounds was conducted: their thermodynamic properties as well as their electrochemical cycling properties are presented. Based on our study of corrosion and solid-gas cycling properties, we are able to understand if the capacity decrease upon electrochemical cycling is due to loss of crystallinity or corrosion.

II. Experiment

High purity yttrium (Santoku, 99.9 %), gadolinium (Alfa Aesar, 99,9%), samarium (Alfa Aesar, 99,9%) and nickel (Praxair, 99.95 %) were used to synthesize Y_2Ni_7, Gd_2Ni_7 and Sm_2Ni_7. For Y_2Ni_7 and Gd_2Ni_7, the elements were melted several times in an induction furnace under controlled atmosphere to obtain homogeneous 8 g. ingots. Subsequent annealing was performed for 7 days at 1000°C in a silica tube under argon atmosphere before quenching in water to room temperature. Because of the high volatility of samarium, Sm_2Ni_7 was synthesized in a different way. A small excess of samarium was added before the successive fusions in the induction furnace. Weight was monitored between each fusion assuming that the weight loss was due to samarium. Once the ratio Sm/Ni reached 2/7, the button was crushed into powder (< 100 µm). It was then pressed into a pellet, wrapped in a tantalum foil and introduced into a stainless steel crucible. Finally, it was annealed at 950°C for 3 days and quenched at room temperature.

X-ray diffraction (XRD) was performed using a Bruker D8 DA VINCI diffractometer with a Cu-Kα radiation, in a 2θ-range from 10 to 110° with a step size of 0.01°.

Chemical composition was checked with Electron Probe Microanalysis (EPMA) using a CAMECA SX-100. Bulk samples were mechanically polished to 0.25 µm, using diamond abrasive tape.

P-c isotherms were measured using Sievert's method. The alloys were crushed into powder (< 100 µm), placed in a sample holder under primary vacuum and connected to a hydrogenation rig with gauged volumes. A known pressure of hydrogen gas is introduced in the rig and the pressure decrease is monitored in time. Using NIST equation, the amount of absorbed hydrogen is deduced from the pressure variations. Similar process was followed to measure desorption properties.

To evaluate cyclability of the hydride formation, solid-gas measurements were performed. A sample holder containing the alloy was connected to a hydrogenation rig. It was exposed to the right amount of hydrogen in order to obtain a final pressure of 0.1 MPa once the

equilibrium state was reached. Then, the sample was fully desorbed by heating at 150 °C under dynamic primary vacuum for a few hours. This procedure was repeated several times.
To prepare the electrode composite, 90 wt% of active material (here Y_2Ni_7, Gd_2Ni_7 or Sm_2Ni_7), 5 wt% of carbon black, the electronic conductor, and 5 wt% of PTFE, the binder, are mixed together. It is spread out in a sheet of 250 µm in thickness. The resulting tape is dried under vacuum overnight. It is then cut in two squares of 5 mm sides. Those squares are pressed on both sides of a nickel grid, the current collector, to form the negative electrode. Two sintered $NiOOH/Ni(OH)_2$ plates were used as a positive electrode. The two electrodes were separated by a nonwoven material in polypropylene and immersed in the electrolyte, a KOH solution at 8.7 M. Open cells were charged and discharged at a C/10 rate at room temperature, where C is the expected alloy capacity calculated from *P-c* isotherm up to 0.1 MPa. The charge duration was 11 hours to assume 10% overcharge, and the end of discharge was set to a cutoff limit at -0.6V versus Hg/HgO.
To study calendar corrosion, 100 µm size powder was divided into several 200 mg-samples. Those samples were immersed in the same solution (*i.e.* 8.7 M KOH solution) and put in a climate oven at 25°C under continuously renewed argon atmosphere. The different times of storage are: 3, 5.5, 9, 24, 48, 168, 672, 840, 1344, 3024, and 9744 hours. To stop the corrosion reaction, the powder was rinsed with a low concentrated KOH solution (10^{-2} M). It corresponds to pH 12 to avoid dissolving the corrosion products. Then, the sample was dried under dynamic vacuum at 40°C for 24 hours. The obtained powder was characterized by XRD, SEM (Scanning Electronic Microscopy), TEM (Transmission Electronic Microscopy), Raman micro-spectroscopy and magnetic measurements.
The corroded samples were first observed by SEM using a MERLIN II from Carl Zeiss. Two different preparations were followed. The first one consisted in spreading out the sample on a double-sided carbon tape stuck on a SEM stub. The most corroded samples were coated with a 2.5 nm-thick Pt/Pd layer. The aim was to observe the surface of the grains. The second procedure consisted in embedding the corroded grains in a resin. The resin and grains were cut using a diamond knife blade. Finally, the sample was coated with a 2.5 nm-thick Pt/Pd layer. This method allows to see a cross-section of the non-corroded core and the external corrosion products. Those samples were investigated using several detectors: SE2 (morphology), EDX (chemical composition), BSE (chemical composition) and EBSD (crystallographic orientation).

TEM (Transmission Electron Microscopy) was performed using a Tecnai FEI F20 ST providing high spatial resolution imaging of the scale morphology, crystallography (by electron diffraction) and chemistry (by EDX analyses) of the corrosion products. TEM specimens were prepared by cutting with an ultra-microtome thin slices (60 to 80 nm) of a resin embedding powder particles.

Raman micro-spectroscopy was performed using Notch filter based micro-spectrometer equipped with Peltier cooled CCD (Horiba Jobin Yvon) with a focal length of 180 mm, a 1800 lines mm^{-1} grating and a He-Ne laser emitting at 632.8 nm. Spectral resolution is around 3 cm^{-1} and calibration is checked on the 520.5 cm^{-1} band of silicon. Microanalysis is achieved through Olympus microscope and 100x Olympus objective with a beam size about 2 µm. A

laser excitation power of 70 µW is used. Spectrum acquisitions are managed by the LabSpec software (Horiba Jobin Yvon).

Magnetic measurements were recorded at 300K with a field up to 9T using a Physical Properties Measurement System (PPMS) from Quantum Design. A small quantity of alloy was used: from 20 to 60 mg depending on the signal strength, as massive sample or powder fixed by a resin.

III. Results

1. Phase determination and structural properties

   Y_2Ni_7, Gd_2Ni_7 and Sm_2Ni_7 were characterized by means of XRD (X-ray diffraction) and EPMA (Electron Probe Microanalysis). Those techniques confirmed that the alloys are pure A_2B_7-type but with two polymorphs. Table 1 summarizes the proportion of Gd_2Co_7-type and Ce_2Ni_7-type polymorphs for the three alloys. More detailed results concerning Y_2Ni_7 have been presented in a previous article [13].

Table 1: Results of EPMA and XRD characterizations for Y_2Ni_7, Gd_2Ni_7 and Sm_2Ni_7.

	EPMA composition	Gd_2Co_7-type (*R*) (wt.%) (XRD)	Ce_2Ni_7-type (*H*) (wt.%) (XRD)
Y_2Ni_7	$Y_2Ni_{6.92(1)}$	100	0
Gd_2Ni_7	$Gd_2Ni_{6.93(1)}$	63 (1)	37 (1)
Sm_2Ni_7	$Sm_2Ni_{6.91(1)}$	21 (1)	79 (1)

2. Thermodynamic properties

The *P-c* isotherms of Y_2Ni_7, Gd_2Ni_7 and Sm_2Ni_7 measured at 25°C are shown in Figure 1. The *P-c* isotherm of Y_2Ni_7, with a maximum pressure applied around 10 MPa (Figure 1a), was previously described [13]. It exhibits three plateau pressures whereas for Gd_2Ni_7 and Sm_2Ni_7 only two plateaus are observed. For Gd_2Ni_7, the first one appears at 0.08 MPa and the corresponding hydrogen content is between 0.7 and 3.6 H/f.u. The second plateau is located around 5 MPa for a capacity between 5.2 and 9.2. For Sm_2Ni_7, the first plateau appears at 0.01 MPa ranging between 0.1 and 3.7 H/f.u. The second plateau pressure is approximately 7 MPa, it corresponds to a capacity between 5.1 and 9.3 H/f.u. The fully charged Gd_2Ni_7 and Sm_2Ni_7 hydrides do not desorb hydrogen. However, *P-c* isotherms measured in the range 0.001 and 0.1 MPa show reversibility (Figure 1b). From these low pressure *P-c* isotherms, it is possible to estimate the reversible capacity in open cells (for a pressure range between 0.001 and 0.1 MPa): 98 mAh g^{-1} for Y_2Ni_7, 115 mAh g^{-1} for Gd_2Ni_7 and 180 mAh g^{-1} for Sm_2Ni_7.

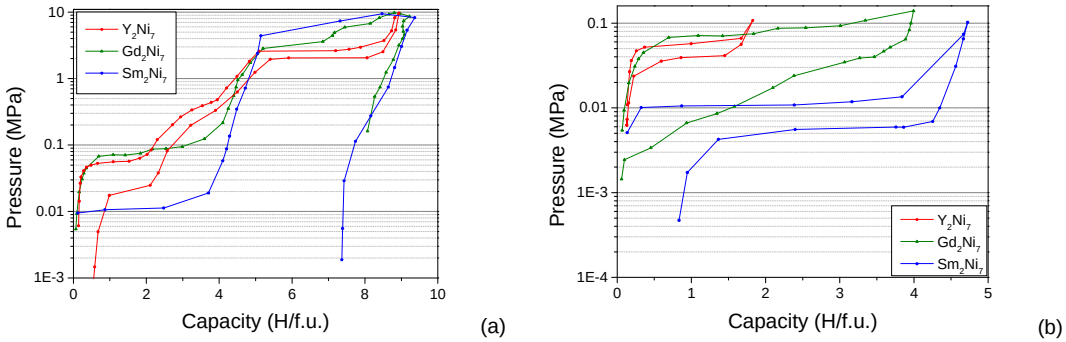

Figure 1: *P-c* isotherms (absorption and desorption) measured at 25°C for Y_2Ni_7 [13], Gd_2Ni_7 and Sm_2Ni_7, with maximum applied pressure of 10 MPa (a) and 0.1 MPa (b)

3. Cycling behavior

Electrochemical cycling behaviors for Y_2Ni_7, Gd_2Ni_7 and Sm_2Ni_7 are compared in Figure 2a. The maximal capacity is 105 mAh g^{-1} for Y_2Ni_7, 93 mAh g^{-1} for Gd_2Ni_7 and 170 mAh g^{-1} for Sm_2Ni_7. For Y_2Ni_7, the capacity remains constant during the first ten cycles then quickly diminishes between cycle 10 and cycle 30 to finally diminish slightly beyond cycle 30. For Gd_2Ni_7, electrochemical capacity drops for the first fifth cycles, then diminishes slightly. For Sm_2Ni_7, capacity drops quickly from cycle 2 to cycle 25 (75% lost), and then it keeps on decreasing more slightly.

For Y_2Ni_7 (Figure 2b), Gd_2Ni_7 (Figure 2c) and Sm_2Ni_7 (Figure 2d), the cycling capacity is compared to solid-gas measurements. Three different behaviors are observed: for Y_2Ni_7, the solid-gas capacity remains remarkably constant even after 80 cycles (this behavior has been already described in Ref. 13) ; for Gd_2Ni_7, both solid-gas and electrochemical capacities are very close (except for the first cycle), and for Sm_2Ni_7, the solid gas capacity drops from 180 to 37 mAh g^{-1} in only 10 cycles. For Sm_2Ni_7, it is surprising that the capacity decay is larger for solid-gas measurements than for electrochemical ones. However, Latroche and Percheron-Guégan reported that if hydrogen is absorbed incrementally, then it is possible to avoid amorphization [14]. For our solid-gas measurements a large amount of hydrogen was introduced at once for each cycle, whereas in electrochemical measurements hydrogen is slowly absorbed for several hours. It may explain the significant capacity decay in solid-gas measurements. X-ray diffraction patterns obtained after solid-gas cycling are presented in Supporting Information (Figure S1, Supporting information). For Gd_2Ni_7 and Sm_2Ni_7, peak broadening is observed indicating that the main structures are preserved with a severe loss in crystallinity. This seems more significant for Sm_2Ni_7. For Y_2Ni_7, even after 80 cycles, the structure is fully preserved. Indeed there is no peak broadening or shift of the diagram in 2θ.

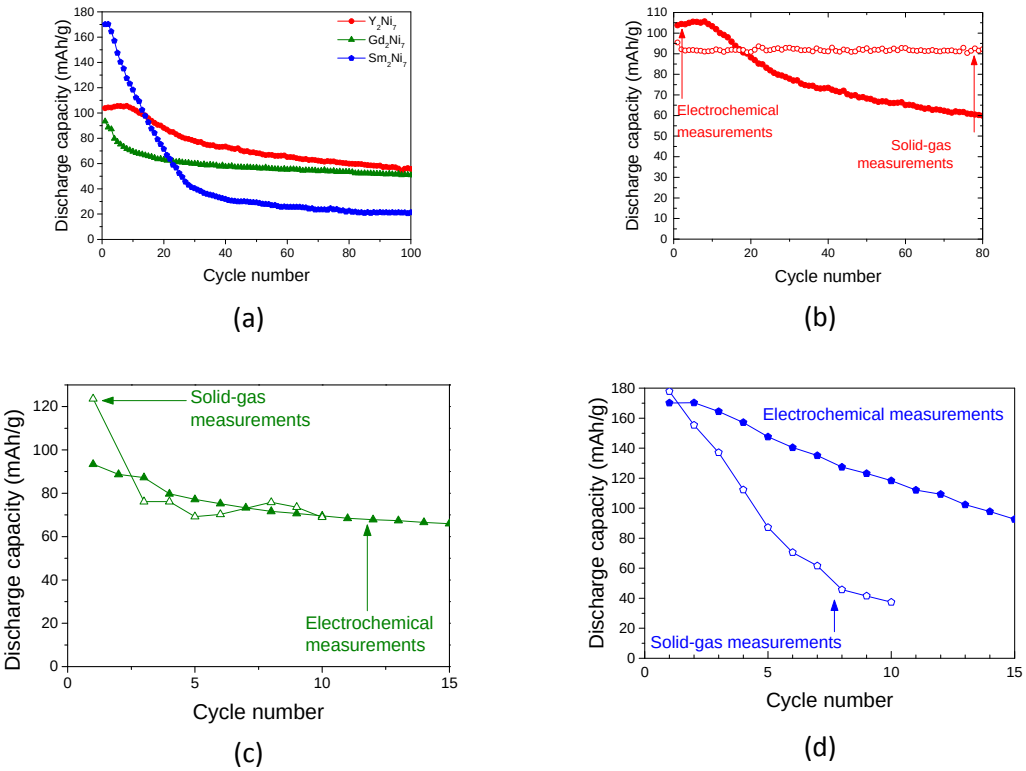

Figure 2: Electrochemical and solid-gas cycling for the three alloys at room temperature. Electrochemical cycling behavior for Y_2Ni_7, Gd_2Ni_7 and Sm_2Ni_7 (a), comparison of electrochemical and solid-gas cycling for Y_2Ni_7 (b), Gd_2Ni_7 (c) and Sm_2Ni_7 (d).

4. Calendar corrosion

XRD analysis was performed for calendar corrosion at various times for each alloy (Figure 3). It is worth to notice that no KOH was identified. For short storage times (3 to 9h), no difference is observed with fresh A_2Ni_7 (A = Y, Gd or Sm). After one day of storage, the first diffraction peaks corresponding to yttrium or rare earth hydroxide $A(OH)_3$ appear. The more the elapsed time increases, the more their diffraction peak intensity increases. The peaks are quite sharp, which means the hydroxide is well crystallized. In contrast, a broad peak corresponding to metallic Ni is observed for the Y_2Ni_7 samples corroded more than one week and for Sm_2Ni_7 and Gd_2Ni_7 corroded 18 weeks. XRD pattern of Y_2Ni_7 corroded 18 weeks was refined (Figure 3b) by Rietveld method using FullProf program [15]. Nickel with *Fm*-3*m* cubic structure (a = 3.52657(9) Å) and crystalline size about 6 nm was identified.

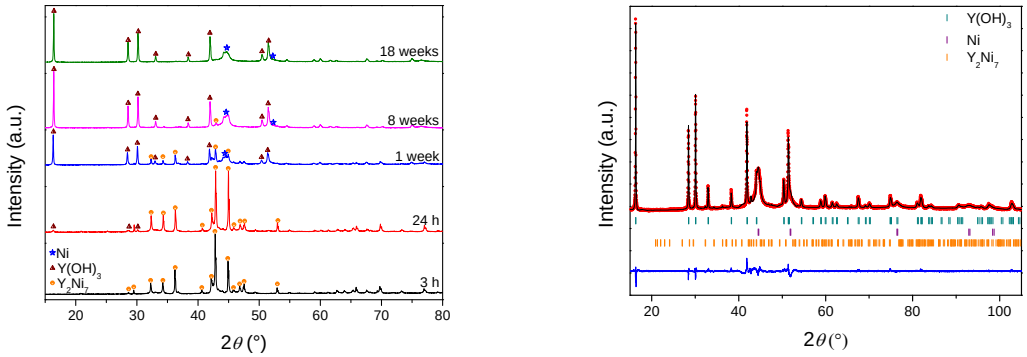

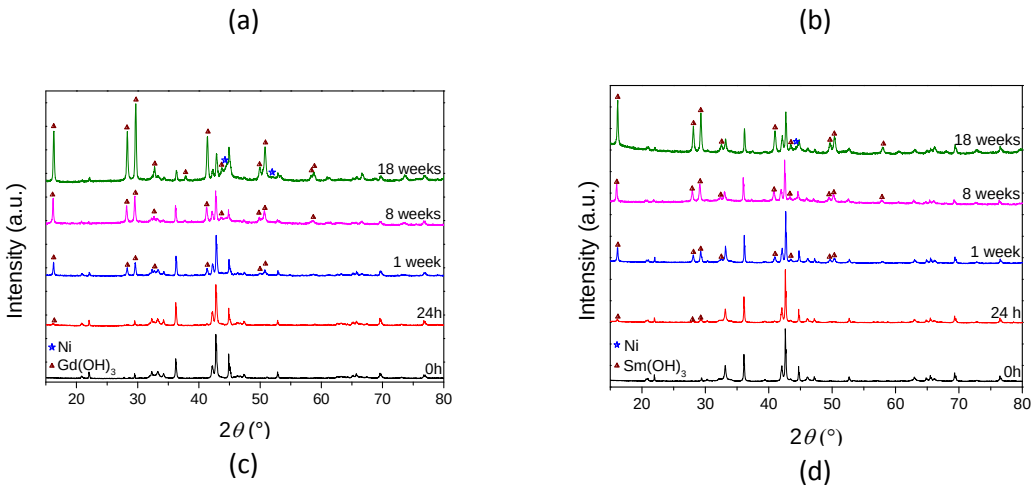

Figure 3: XRD patterns of Y_2Ni_7 (a), Gd_2Ni_7 (c) and Sm_2Ni_7 (d) after different corrosion times in potassium hydroxide solution of 8.7 M. Refined XRD pattern of Y_2Ni_7 corroded 18 weeks (b).

Presence of $A(OH)_3$ was also confirmed by Raman spectroscopy (Figure S2, Supporting Information). In the case of Y_2Ni_7, numerous Raman spectra were recorded for different corrosion times and no nickel- rich corrosion products can be identified (Figure S2a). For Gd_2Ni_7 and Sm_2Ni_7, in addition to $A(OH)_3$, nickel hydroxide $Ni(OH)_2$ was recognized after 18 weeks of corrosion. Indeed the two black spectra in Figure S2b and c present large peaks, when the laser is focalized on black spots located at the surface of the grain. Those large peaks correspond to the convolution of $A(OH)_3$ and $Ni(OH)_2$ Raman signals.

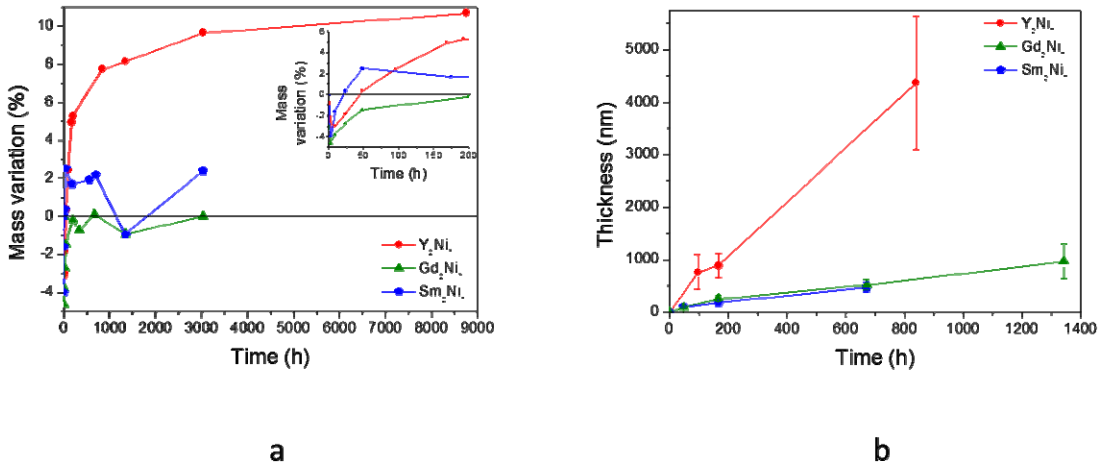

Figure 4: (a) Mass variation of Y_2Ni_7, Gd_2Ni_7 and Sm_2Ni_7 as a function of corrosion time in potassium hydroxide solution at 8.7 M. Mass variation errors are not represented but they are around 4% for less-corroded compounds and diminish in time; (b) Thickness variation of the Ni layer formed on Y_2Ni_7, Gd_2Ni_7 and Sm_2Ni_7 as a function of corrosion time. Thickness was measured from sectional views of the grains observed by SEM.

Mass variation of Y_2Ni_7, Gd_2Ni_7 and Sm_2Ni_7 as a function of corrosion time is presented in Figure 4a. This variation can be described in three steps. The first step happens during the

very first hours of corrosion where a mass loss is observed. We attributed that to the unavoidable loss of floating grains of alloy during the rinsing step. To confirm this, six 200 mg powder samples were immersed in electrolyte and rinsed immediately. The average weight loss was about 4.0 mg ± 1.8 %. However, this weight loss is not steady. Indeed after a while, all grains have sunk to the bottom of the pillbox, aggregates are formed, and a smaller amount of grains is removed accidentally. The second step consists in a large mass increase. This is due to the formation of hydroxide crystals. SEM analysis confirmed that those crystals are stuck on the alloy surface (Figure 5a, b and c). During the final step, the mass gain is slow which indicates that the corrosion speed stabilizes. It is worth to note that for Gd_2Ni_7 and Sm_2Ni_7, the experimental errors and the mass increase are of the same order. For Y_2Ni_7, the mass increase caused by hydroxide formation is much larger than experimental errors.

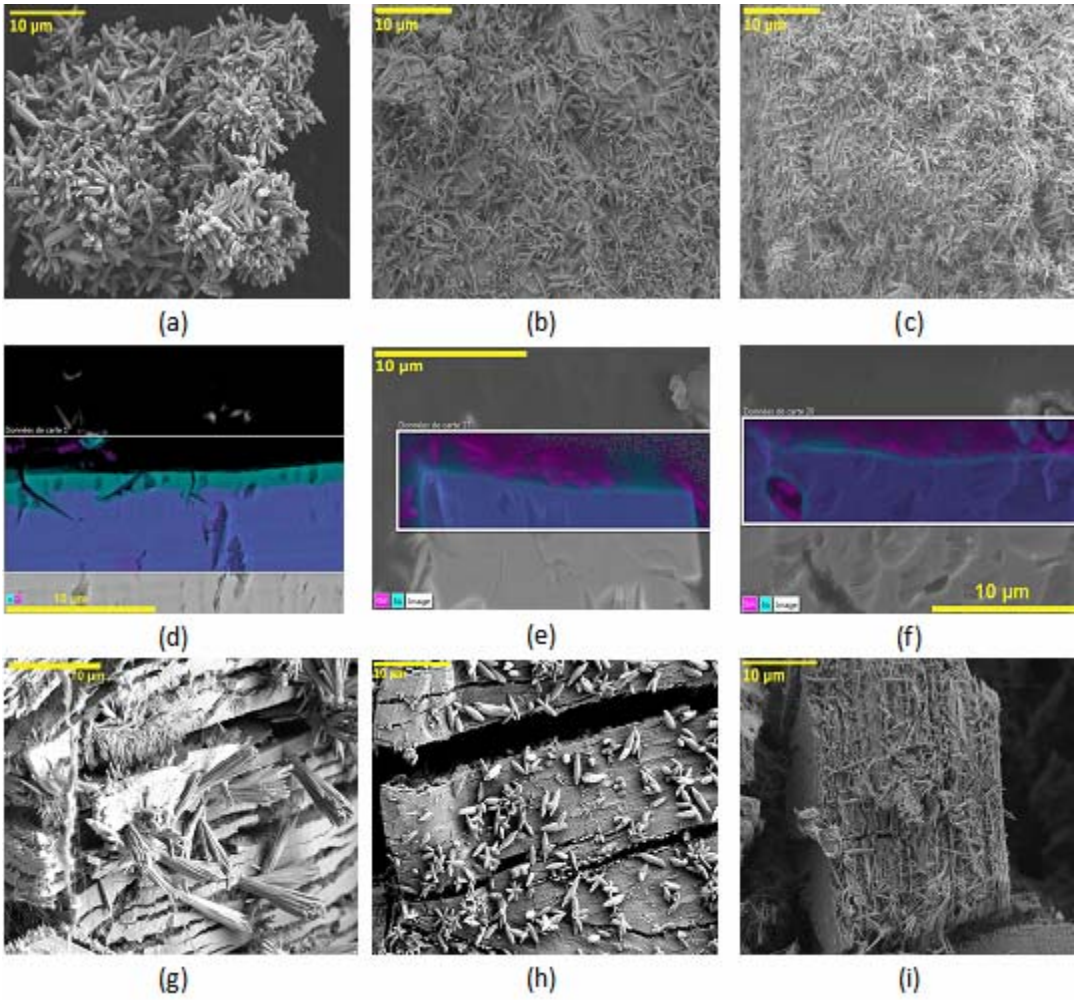

Figure 5: SEM micrographs of Y_2Ni_7 (a, d), Gd_2Ni_7 (b, e) and Sm_2Ni_7 (c, f) corroded 1 week and Y_2Ni_7 (g), Gd_2Ni_7 (h) and Sm_2Ni_7 (i) after respectively 180, 200 and 180 electrochemical cycles. (a), (b), (c), (g), (h) and (i) micrographs are in SE2 mode and present the surface of the grains. (d), (e) and (f) micrographs are in BSE mode and present a sectional view of the grains.

SEM-EDX elemental map of Y_2Ni_7 corroded 48h is presented in Figure S3 (Supporting Information). Yttrium is clearly located in the corrosion products deposited at the surface of the grain. From XRD results, we know that the needles are made of $Y(OH)_3$. The surface of

the grain is mainly composed of nickel. Figure 5a, b and c show that the three alloys form needles upon corrosion.

TEM analysis was performed on a sectional view of Y_2Ni_7 corroded for 48 hours (Figure S4, Supporting Information). A STEM-EDX elemental profile was recorded perpendicularly to the surface of the grain. Two different layers were identified. The first is a nickel-rich one that covers the whole surface, the second is formed of yttrium-rich micrometric particles deposited on top of the first layer. SEM-EDX elemental maps of sectional views of the grains are presented in Figure 5d, e and f. The darker parts at the top of the micrographs correspond to the resin used to embed the samples. On the surface of the grains a nickel rich layer is observed and on the top of it, rare earth (or yttrium) rich needles are present, $A(OH)_3$. It confirms the results obtained from TEM analysis and shows that Y_2Ni_7, Gd_2Ni_7 and Sm_2Ni_7 have similar behavior during calendar corrosion.

An electron diffraction pattern was recorded for the nickel rich layer of Y_2Ni_7 corroded one week (Figure S5, Supporting Information). It can be indexed using nickel cubic structure (space group *Fm*-3*m*). The unit cell parameter was found to be 0.352(2) nm. It is close to the one obtained from Rietveld refinement of the diffraction pattern of Y_2Ni_7 corroded 18 weeks (Figure 3b). Furthermore, the electron diffraction pattern presents diffraction rings which confirm that nanometric size of the cubic nickel particles composing the nickel rich layer.

Sectional views of the grains observed in BSE mode were used to measure thickness of the nickel rich layer. The results are presented as a function of corrosion time in **Erreur ! Source du renvoi introuvable.**. Error bars are important since the thickness is not constant at the alloy surface. It grows faster for Y_2Ni_7 than for Gd_2Ni_7 and Sm_2Ni_7. It is around 4 µm for Y_2Ni_7 corroded five weeks whereas it is close to 500 nm for Gd_2Ni_7 and Sm_2Ni_7 corroded four weeks. Up to now, XRD patterns (Figure 3), mass variation (Figure 4a) and evolution of the thickness layer (Figure 4b) show that Y_2Ni_7 corrodes faster than Gd_2Ni_7 and Sm_2Ni_7.

To get a better estimation of the corrosion rate, we performed magnetic measurements. Those measurements are based on the magnetic properties of Y_2Ni_7, Gd_2Ni_7, Sm_2Ni_7 and cubic nickel. The three studied alloys are paramagnetic at ambient temperature, whereas cubic nickel is ferromagnetic. Figure 6 shows the magnetization curves of non-corroded Y_2Ni_7 (a), Gd_2Ni_7 (b) and Sm_2Ni_7 (c), corroded 1 week and corroded 8 weeks. It is worth to note that intrinsic properties of Gd_2Ni_7 do not lead to saturation in contrast to Y_2Ni_7 and Sm_2Ni_7. This larger slope for Gd_2Ni_7 can be attributed to the strong paramagnetic contribution of Gd ($\mu(Gd) = 7.94\ \mu_B$ toward $\mu(Sm) = 1.54\ \mu_B$). However, the important feature is related to the stepped increase of the magnetization as a function of corrosion time.

Ayari *et al.* claim that $La(OH)_3$ has a weak paramagnetic contribution [16]. Therefore the hydroxides contribution to magnetism was not taken into account in our calculation. From saturation magnetization of nickel (53 $Am^2\ kg^{-1}$ [17]) and from magnetization curves of non-corroded A_2Ni_7, we deduced the mass of nickel present in the corroded A_2Ni_7. It is represented in Figure 6d and compared to mass variations (Figure 4a) assuming that the

mass variation is only due to the formation of $A(OH)_3$. Figure 6d shows that similar results are obtained by the two methods. They both show that Y_2Ni_7 corrodes faster than Gd_2Ni_7 and Sm_2Ni_7 and that a steady state appears at long corrosion time. Gd_2Ni_7 and Sm_2Ni_7 have similar corrosion rates, in agreement with the thickness variation of the corrosion layer. We assumed that the $Ni(OH)_2$ contribution is negligible compared to metallic nickel one.

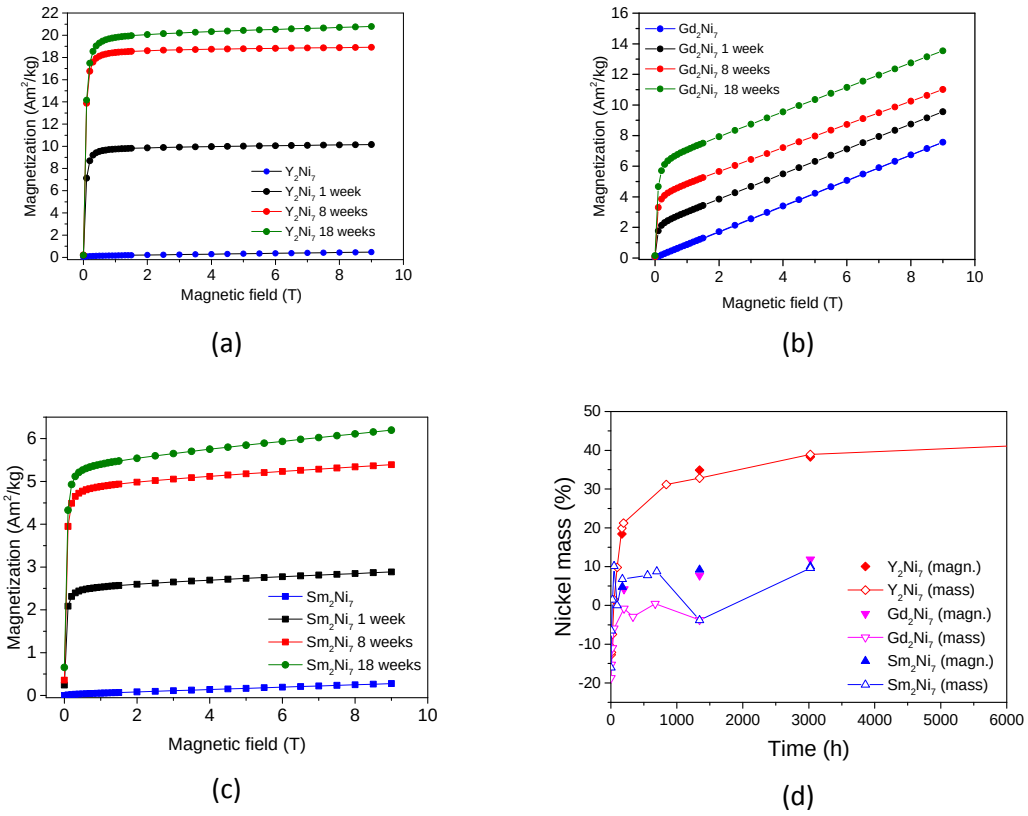

Figure 6: Magnetization curves of Y_2Ni_7 (a), Gd_2Ni_7 (b) and Sm_2Ni_7 (c) and the corresponding corroded samples after 1 and 8 weeks in KOH solution. Measurements were performed at 25°C. Evolution of the nickel mass as a function of corrosion time derived from mass variation (hollow symbols) and magnetic measurements (solid symbol) (d).

5. Corrosion in cycling conditions

SEM micrographs of Y_2Ni_7, Gd_2Ni_7 and Sm_2Ni_7 after electrochemical cycling are shown respectively in Figure 5g, h and i. Decrepitation of the grains occurred. For the three compounds, the grains crack into slices. $A(OH)_3$ needles form on the newly created surfaces. To identify the crack orientation, EBSD analysis was performed for Gd_2Ni_7 after electrochemical cycling (Figure 7). Figure 7a shows a sectional view of Gd_2Ni_7 after electrochemical cycling, three parallel cracks are clearly observed. Figure 7b is an EBSD inverse pole figure map of that grain. On this map the colors are related to a specific crystallographic orientation. The grain appears fully red which means that it is a single crystallite. Pole figures are presented on Figure 7c. The left one, associated to direction [0001], shows that the cracks are perpendicular to the *c*-axis.

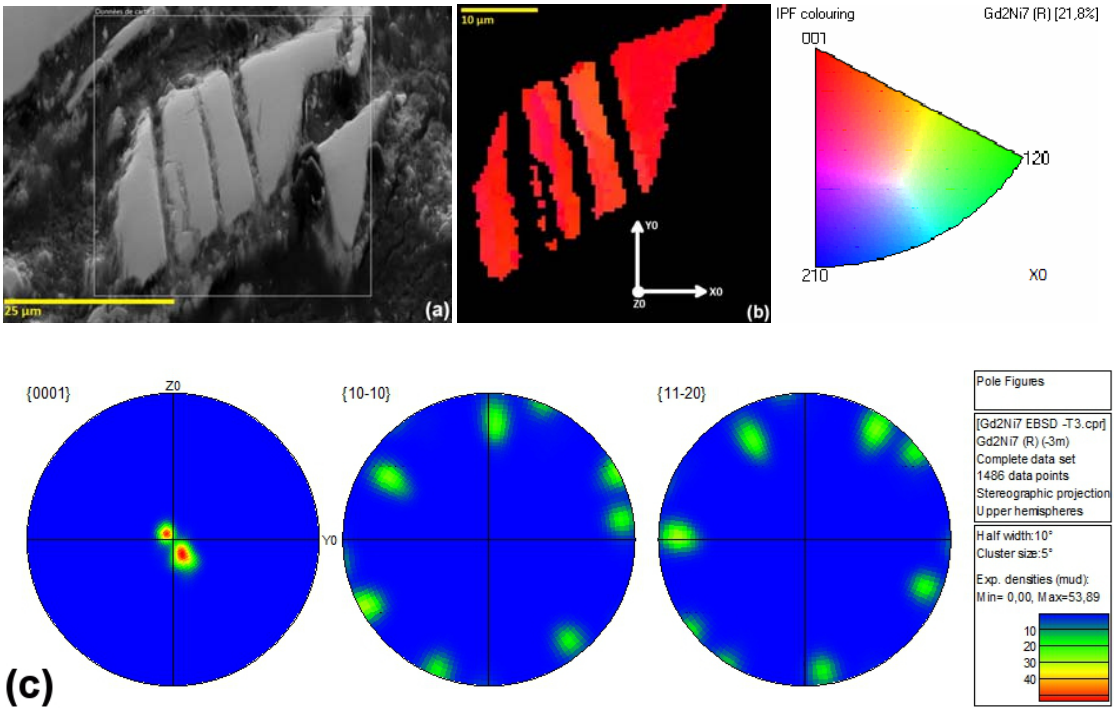

Figure 7: EBSD analysis performed on Gd_2Ni_7 after electrochemical cycling. (a) SEM micrograph in SE2 mode of a sectional view of a grain of Gd_2Ni_7 after electrochemical cycling, (b) EBSD inverse pole figure map of rhombohedral Gd_2Ni_7 and (c) Pole figures of the [0001], [10-10] and [11-20] directions of all measured points (pixels of the map (b)).

XRD patterns of the composite electrodes before and after electrochemical cycling are presented in Figure 8. Electrochemical cycling lasted approximately 18 weeks. For sake of comparison, XRD patterns of A_2Ni_7 corroded 18 weeks in KOH solution was also added to Figure 8. $A(OH)_3$ and Ni were indexed after calendar corrosion as well as cycling corrosion. For Y_2Ni_7, no peak broadening is observed and there is no shift of the diagrams in 2θ for both calendar and cycling corrosions. For the electrochemically cycled sample, the amount of $Y(OH)_3$ is less than after 18 weeks in KOH. In the case of Gd_2Ni_7, diffraction peaks corresponding to the active material are broader after electrochemical cycling. For the electrochemically cycled Sm_2Ni_7 sample, no diffraction peak of the active material is observed. Nevertheless, the main diffraction halo around 42.9° coincides with the main diffraction peak of Sm_2Ni_7, a loss of crystallinity of the active material occurred. Diffraction peaks of $Sm(OH)_3$ and cubic nickel are also identified.

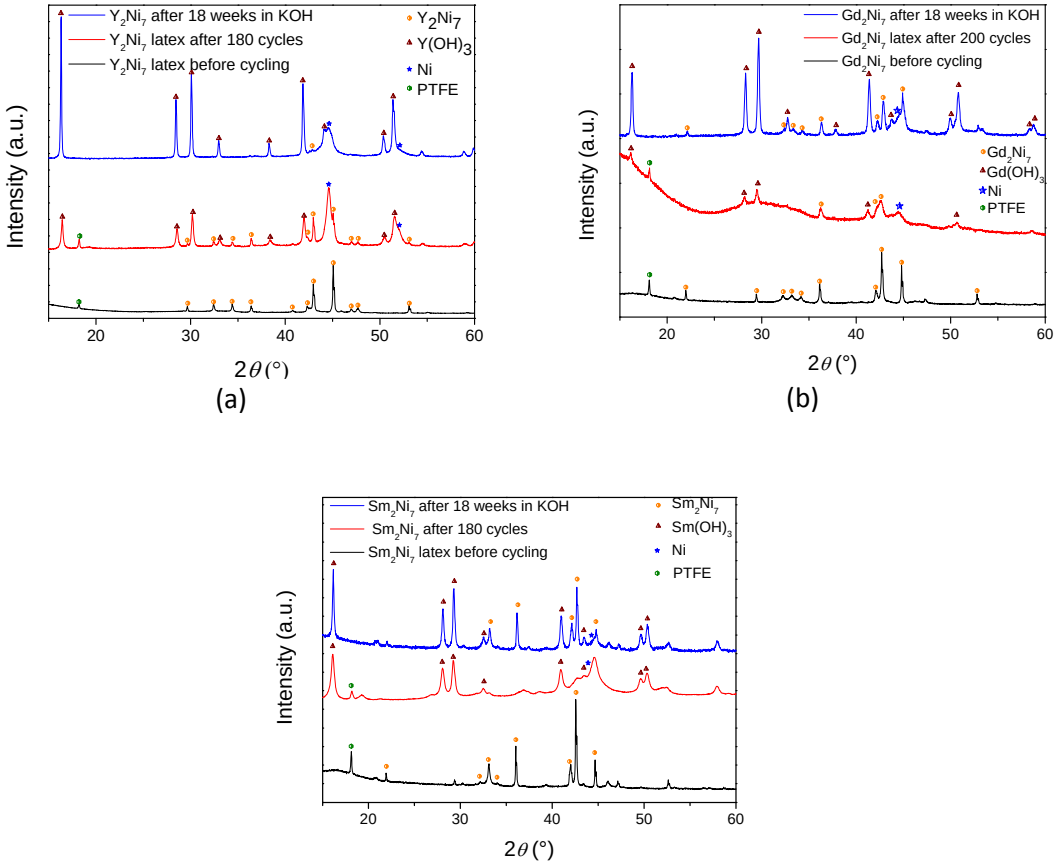

Figure 8: XRD patterns of Y_2Ni_7 (a), Gd_2Ni_7 (b) and Sm_2Ni_7 (c) corroded 18 weeks in KOH solution and Y_2Ni_7 (a), Gd_2Ni_7 (b) and Sm_2Ni_7 (c) composite electrodes before and after electrochemical cycling (equivalent to 18 weeks of cycling).

IV. Discussion

Decrepitation:

Decrepitation is the reduction into smaller grains of the active material during hydrogenation cycling. It occurs both in solid-gas and electrochemical processes. In the present work, unusual crystallographically oriented decrepitation of the grains occurs. Indeed, the grains cracks are parallel to each other. For AB_5-type alloys, after cycling, cracks are orientated randomly [8,18–20]. EBSD performed on Gd_2Ni_7 showed that the cracks are perpendicular to the *c*-axis (Figure 7). For AB_x-type alloys (x=3; 3.5 and 3.8), uniaxial expansion of the structure along the *c*-axis during hydrogenation is often observed in the literature [21–24]. During hydrogenation, Y_2Ni_7 [13] and Gd_2Ni_7 (Figure S6 and Table S1, Supporting Information) also undergo anisotropic expansion along the *c*-axis. This phenomenon was explained by the fact that during the first step of hydrogenation, only $[A_2B_4]$ subunits host hydrogen involving a volume increase. However, the hydrogen-free neighboring $[AB_5]$ subunits tend to keep their own volume constraining the *ab* basal plane. Accordingly, the $[A_2B_4]$ subunits can only grow

along the *c*-axis in these intergrowth structures [25]. This creates weaker atomic bonds along this crystallographic axis leading to the formation of cracks perpendicular to the *c*-axis.

Corrosion products:

$A(OH)_3$ hydroxide formation was identified by both Raman spectroscopy and X-ray diffraction as a corrosion product of A_2Ni_7 (*A* = Y, Gd or Sm). Cubic nickel with space group *Fm*-3*m* was also found to crystallize on the surface of the three compounds (XRD and electron diffraction). Thanks to Raman spectroscopy, $Ni(OH)_2$ was identified as another corrosion product for Gd_2Ni_7 and Sm_2Ni_7 for longer soaking times. SEM-EDX presented in Figures S7, S8 and S9 (Supporting Information) show that oxygen is present in this nickel-rich layer. It is then possible that NiO passivates the surface of the cubic nickel nanoparticles. However no NiO was identified by X-ray diffraction and we conclude that NiO is present in very small amount. For Y_2Ni_7, the global reaction occurring during corrosion can be written as

$$Y_2Ni_7 + 6H_2O \rightarrow 2Y(OH)_3 + 7Ni + 3H_2 \qquad (1)$$

These results are in agreement with literature. In addition to rare earth hydroxides, Maurel *et al.* [26] observed the formation of a (Ni,Co) solid solution layer with some (Ni,Co)O oxide at the surface of the grains of $MmNi_{3.55}Co_{0.75}Mn_{0.4}Al_{0.3}$ during calendar corrosion. Typical grain sizes of these solid solutions were about 10 to 20 nm according to TEM analysis. Li *et al.* [27] also studied corrosion of $MmNi_{3.55}Co_{0.75}Mn_{0.4}Al_{0.3}$. The alloy was immersed in an alkaline solution (15 M) at 110 °C for different times. They observed rare earth hydroxides as well as Ni clusters. Performing TEM observations and magnetic measurements, the Ni clusters average diameter was found to be around 9 nm after 110 minutes.

However, these authors did not identified $Ni(OH)_2$ that we reported here by Raman spectroscopy for Gd_2Ni_7 and Sm_2Ni_7 corroded 18 weeks. This may be due to the low corrosion time studied: maximal corrosion time 110 minutes for Li *et al.* [27] and 12 weeks for Maurel *et al.* [26]. However, Monnier *et al.* [28] studied calendar corrosion of La_2Ni_7 following the same experimental method that we did and they clearly observed $Ni(OH)_2$ after 48 hours using STEM-EDX, XRD and Raman spectroscopy. Then it seems that the nature of the rare earth determines the nature of the corrosion products. Concerning Li *et al.* [27], they concentrated their study on morphological analyses of the (Ni,Co)O oxide but did not use Raman spectroscopy neither SEM-EDX or STEM-EDX mapping. Without these techniques it is not possible to identify whether $Ni(OH)_2$ is present or not. The presence of $Ni(OH)_2$ could be explained by partial hydrolysis of the NiO passivation scale.

Electrochemical cycling:

Losses of capacity during electrochemical cycling are attributed to cycling inducing decrepitation that accelerates corrosion. The present work reports the remarkable cycling properties of Y_2Ni_7. Indeed, solid-gas capacity remains constant for at least 80 cycles (Figure 2b) and XRD pattern recorded after solid-gas cycling does not show any peak broadening and no shift of the diffraction line in 2θ (Figure S1a, Supporting Information). Similarly, after electrochemical measurement, XRD shows that the structure of Y_2Ni_7 is preserved (Figure

8a). Therefore, the decrease in capacity of that compound is mainly due to corrosion and not to crystallinity loss.

As concerns Gd_2Ni_7 and Sm_2Ni_7, XRD patterns after solid-gas (Figure S1b and c, Supporting Information) and electrochemical cycling (Figure 8b and c) show some amorphization process. In spite of their low calendar corrosion rate (Figure 4 and Figure 6d), the capacity decreases faster for Gd_2Ni_7 and Sm_2Ni_7 than for Y_2Ni_7. This faster capacity loss is then mainly attributed to crystallinity loss as it yields to the irreversibility of hydrogen absorption [9,29].

According to XRD, the amount of $A(OH)_3$ seems to be smaller after electrochemical cycling than after 18 weeks in KOH. This is in good agreement with SEM micrographs, since after only one week (Figure 5a, b and c) there are more needles than after 18 weeks of electrochemical cycling (Figure 5g, h and i). In a first approach, it contradicts the fact that decrepitation enhances corrosion. However, during electrochemical cycling, successive volumetric expansion and reduction is imposed to the active material. It probably breaks down most of the corrosion products which fall in the electrolyte solution, which also explains the small size of the needles.

Corrosion mechanism:

Different corrosion mechanisms have been proposed.

- Out-Diffusion of *A*

  Willems *et al.* studied different lanthanum based AB_5-type electrodes. They observed $La(OH)_3$ needles at the surface and a lanthanum depleted area below. They noticed that corrosion took place only for continuously charged and discharged electrodes and focused to volume changes during hydride formation and desorption that could form short-circuit diffusion path [1]. Therefore they proposed a mechanism implying the diffusion of lanthanum atoms through active material to the surface. Once at the surface, lanthanum reacts with hydroxide anion to form $La(OH)_3$.

  However, we clearly observed here corrosion during both calendar and cycling corrosion. This is in accordance with Maurel *et al.* [26], who observed the same corrosion products in calendar or cycling corrosion. Furthermore, the nickel rich layer is very thick and diffusion of *A* in metallic state is too slow compared to our corrosion rates.

- A^{3+} and HO^- counterdiffusion

  Maurel *et al.* [26] claimed that both A^{3+} and HO^- diffusions occur through the Ni surface layer (Figure S10, Supporting Information). This mechanism is supported by the present results. SEM-EDX showed that oxygen is present in the nickel-rich layer (Figures S7, S8 and S9, Supporting Information). It indicates that HO^- is able to penetrate into this layer. For Gd_2Ni_7 and Sm_2Ni_7, nickel hydroxide was identified (Figure S2, Supporting Information) whereas for Y_2Ni_7, no nickel oxide or hydroxide was found. However, Puga *et al.* [30] report by impedance spectroscopy measurements that an oxide forms upon corrosion for Y_2Ni_7 and Gd_2Ni_7. It is probably some nickel oxide embedded into the porous nickel layer.

A^{3+} diffuses from the A_2Ni_7 compound through the nickel rich layer and finally participates to the growth of hydroxide needles.

Transporting *A* ions toward the surface to form $A(OH)_3$ needles gives rise to a *A*-depleted Ni-rich phase. The volume change between Y_2Ni_7 (769.63 $Å^3$ for 6 formula unit) and Ni (460.95 $Å^3$ for 42 Ni atoms) leads to 40 % void, resulting in the high porosity of the nickel layer. At this stage, it is worth to consider how *A* element is able to cross the Ni-rich phase. Indeed, according to Pourbaix diagrams of samarium, gadolinium and yttrium, A^{3+} doesn't exist in a basic solution [31]. However, most recent publications claimed the existence of other anionic species, especially AOH^{2+} and $A(OH)_2^+$ [32,33]. This leads us to a possible new mechanism.

- $A(OH)_2^+$ and HO^- counter-diffusion

  The nickel rich layer is composed of nickel nanoparticles of about 6 nm in size with 40% of porosity. Consequently, nanochannels are formed between the particles as confirmed by TEM analysis (Figure S11, Supporting Information). HO^- anions are able to enter the nickel porosity (oxygen is present according to STEM-EDX and SEM-EDX). When an HO^- anion arrives near A_2Ni_7, it forms $A(OH)_2^+$. Consumption of HO^- anions leads to a smaller pH value which stabilizes $A(OH)_2^+$ cation. This cation diffuses to the surface of the grain, where pH is higher, consequently it crystallizes into $A(OH)_3$ on the top of the Ni-rich phase.

  According to Maurel *et al.* [26], $A(OH)_3$ hydroxides form needles because the HO^- are adsorbed on the (0001) surface. As a consequence, hydroxides grow along [0001] direction. Then needles can expand from the base or from the tip.

  Monnier *et al.* [28] and Maurel *et al.* [26] observed hydroxide hollow needles at the grain surface. One can make the hypothesis that $A(OH)_2^+$cations diffuse through the nickel rich layer and then along the inner part of the hollow needles to finally crystallizing as $A(OH)_3$ on top of the needle (due to the basic pH) involving the progressive growth of the needle. According to this we shouldn't obtain 500-nm width needles but very thin ones. Figure S3 (Supporting Information) shows pointed tip needles and thanks to higher magnification one can see that they are made up of many very thin needles (Figure S12, Supporting Information). $A(OH)_2^+$ can actually travel between those needles and crystallize at the tip (or on the side of the pointed tip needle) into $A(OH)_3$ and it results in a needle of hexagonal section.

V. Conclusion

Intermetallic compounds Y_2Ni_7, Gd_2Ni_7 and Sm_2Ni_7 were investigated regarding their structural and hydrogen sorption properties. *P-c* isotherms were measured at 25 °C. The expected capacity was found close to the maximal capacity measured by electrochemical cycling, except for Gd_2Ni_7. Electrochemical cycling was compared to solid-gas one for the three compounds. Calendar and cycling corrosion were studied. Same corrosion products are identified for the two types of corrosion. We can conclude that the mechanism is the same.

Corrosion products observed are: $A(OH)_3$ needles and nanoparticles of cubic nickel for the three compounds and $Ni(OH)_2$ for Gd_2Ni_7 and Sm_2Ni_7 only. For Y_2Ni_7, we attributed the subsequent loss in capacity to corrosion. Indeed the capacity remains constant when measured by solid-gas cycling and its corrosion rate is significant. For Gd_2Ni_7 and Sm_2Ni_7, corrosion is less marked. We concluded that loss in capacity is mainly due to loss of crystallinity for those compounds. Mechanism of corrosion is based on in-diffusion of HO^- and out-diffusion of A^{3+}. Substitution of nickel by cobalt would be interesting to improve the stability in terms of amorphization and corrosion. Magnesium substitution for yttrium or rare earth will decrease the plateau pressures and consequently increase the capacity.

Acknowledgements

The research program MALHYCE (ANR-2011-PRGE-006 01) is acknowledged for financial support. The authors would like to thank colleagues from ICMPE: Dr. E. Leroy, for technical assistance in the EPMA analysis, R. Pires for SEM and especially EBSD analysis, V. Lalanne for TEM samples preparation and J. Bourgon for TEM analyses. Dr. V. Vivier from LISE is duly acknowledged for fruitful discussions in the frame of this work.

References

[1] J.J.G. Willems, K.H.J. Buschow, From permanent magnets to rechargeable hydride electrodes, J. -Common Met. 129 (1987) 13–30.
[2] T. Sakai, I. Uehara, H. Ishikawa, J. Alloys Compd. 293-295 (1999) 762–769.
[3] X. Zhang, W. Yin, Y. Chai, M. Zhao, Mater. Sci. Eng. B. 117 (2005) 123–128.
[4] T. Kohno, H. Yoshida, M. Kanda, Hydrogen storage properties of $La(Ni_{0.9}M_{0.1})_3$ alloys, J. Alloys Compd. 363 (2004) 249–252.
[5] M. Tliha, C. Khaldi, S. Boussami, N. Fenineche, O. El-Kedim, H. Mathlouthi, et al., Kinetic and thermodynamic studies of hydrogen storage alloys as negative electrode materials for Ni-MH batteries: a review, J. Solid State Electrochem. 18 (2014) 577–593.
[6] Y. Khan, The crystal structure of R_5Co_{19}, Acta Crystallogr. B. 30 (1974) 1533–1537.
[7] P.H.L. Notten, Rechargeable nickel-metal hydride batteries: a successfull new concept, in: F. Grandjean, G.J. Long, K.H.J. Buschow (Eds.), Interstitial Intermet. Alloys, Kluwer Academic Publishers, Dordrecht, Boston, London, 1995: pp. 150–194.
[8] J.-M. Joubert, M. Latroche, A. Percheron-Guégan, Metallic hydrides II: materials for electrochemical storage, MRS Bull. 27 (2002) 694–698.
[9] K. Aoki, T. Masumoto, Hydrogen-induced amorphisation of intermetallics, J. Alloys Compd. 231 (1995) 20–28.
[10] L. Zhang, S. Han, D. Han, Y. Li, X. Zhao, J. Liu, Phase decomposition and electrochemical properties of single phase $La_{1.6}Mg_{0.4}Ni_7$ alloy, J. Power Sources. 268 (2014) 575–583. doi:10.1016/j.jpowsour.2014.06.093.
[11] B. Guiose, F. Cuevas, B. Décamps, E. Leroy, A. Percheron-Guégan, Microstructural analysis of the ageing of pseudo-binary (Ti,Zr)Ni intermetallic compounds as negative electrodes of Ni-MH batteries, Electrochimica Acta. 54 (2008) 2781–2789.
[12] M. Latroche, V. Paul-Boncour, A. Percheron-Guégan, Structural instability in $RE_{1-x}Ni_2$ compounds and their hydrides (Re=Y, rare earth)., Z. Für Phys. Chem. 179 (1993) 261–268.
[13] V. Charbonnier, J. Zhang, J. Monnier, L. Goubault, P. Bernard, C. Magén, et al., Structural and Hydrogen Storage Properties of Y_2Ni_7 Deuterides Studied by Neutron Powder Diffraction, J. Phys. Chem. C. 119 (2015) 12218–12225. doi:10.1021/acs.jpcc.5b03096.

[14] M. Latroche, A. Percheron-Guégan, Structural and thermodynamic studies of some hydride forming RM_3-type compounds (R-lanthanide, M=transition metal), J. Alloys Compd. 356-357 (2003) 461–468.
[15] J. Rodríguez-Carvajal, Fullprof: a program for Rietveld refinement and pattern matching analysis, Phys. B. 192 (1993) 55–69.
[16] M. Ayari, V. Paul-Boncour, J. Lamloumi, A. Percheron-Guégan, M. Guillot, Study of the aging of $LaNi_{3.55}Mn_{0.4}Al_{0.3}(Co_{1-x}Fe_x)_{0.75}$ (0<=x<=1) compounds in Ni-MH batteries by SEM and Magnetic measurements, J. Magn. Magn. Mater. 288 (2005) 374–383.
[17] M. Ayari, V. Paul-Boncour, J. Lamloumi, A. Percheron-Guégan, Magnetic properties of $LaNi_{3.55}Mn_{0.4}Al_{0.3}Co_{0.75-x}Fe_x$ (x=0,0.35) before and after electrochemical cycles, J. Magn. Magn. Mater. 242-245 (2002) 850–853.
[18] R. Alcántara, C. Audry, B. Knosp, L. Guenne, P. Bernard, Study of decrepitation and corrosion effects of AB_5 alloys used in Ni-MH batteries by X-ray diffraction, step potential electrochemical spectroscopy and impedance spectroscopy, J. New Mater. Electrochem. Syst. 4 (2001) 107–114.
[19] C. Khaldi, S. Boussami, M. Tliha, S. Azizi, N. Fenineche, O. El-Kedim, et al., The effect of the temperature on the electrochemical properties of the hydrogen storage alloy for nickel–metal hydride accumulators, J. Alloys Compd. 574 (2013) 59–66. doi:10.1016/j.jallcom.2013.04.046.
[20] M. Latroche, Structural and thermodynamic properties of metallic hydrides used for energy storage, J. Phys. Chem. Solids. 65 (2004) 517–522.
[21] V.A. Yartys, A.B. Riabov, R.V. Denys, M. Sato, R.G. Delaplane, Novel intermetallic hydrides, J. Alloys Compd. 408-412 (2006) 273–279.
[22] R.V. Denys, V.A. Yartys, M. Sato, A.B. Riabov, R.G. Delaplane, Crystal chemistry and thermodynamic properties of anisotropic $Ce_2Ni_7H_{4.7}$ hydride, J. Solid State Chem. 180 (2007) 2566–2576.
[23] M. Latroche, V. Paul-Boncour, A. Percheron-Guégan, Structural properties of two deuterides $LaY_2Ni_9D_{12.8}$ and $CeY_2Ni_9D_{7.7}$ determined by neutron powder diffraction and X-ray absorption spectroscopy., J. Solid State Chem. 177 (2004) 2541–2548.
[24] J.I. Nakamura, K. Hayakawa, H. Nakamura, Y.E. Akiba, Structural study of the La_4MgNi_{19} hydride by in-situ X-ray and neutron powder diffraction, J. Phys. Chem. C. 113 (2009) 5853–5859.
[25] J.-C. Crivello, J. Zhang, M. Latroche, Structural Stability of AB_y Phases in the (La,Mg)-Ni System Obtained by DFT Calculations, J. Phys. Chem. C. 115 (2011) 25470–25478.
[26] F. Maurel, B. Knosp, M. Backhaus-Ricoult, Characterization of corrosion products of AB_5-type hydrogen storage alloys for nickel-metal hydride batteries, J. Electrochem. Soc. 147 (2000) 78–86.
[27] H.-W. Li, K. Ikeda, Y. Nakamori, S. Orimo, K. Yakushiji, K. Takanashi, et al., Size distribution of precipitated Ni clusters on the surface of an alkaline-treated $LaNi_5$-based alloy, Acta Mater. 55 (2007) 481–485. doi:10.1016/j.actamat.2006.08.035.
[28] J. Monnier, H. Chen, S. Joiret, J. Bourgon, M. Latroche, Identification of a new pseudo-binary hydroxide during calendar corrosion of $(La, Mg)_2Ni_7$-type hydrogen storage alloys for Nickel–Metal Hydride batteries, J. Power Sources. 266 (2014) 162 – 169. doi:http://dx.doi.org/10.1016/j.jpowsour.2014.05.008.
[29] K. Aoki, Amorphous phase formation by hydrogen absorption, Mater. Sci. Eng. A. 304-306 (2001) 45–53.
[30] B. Puga, S. Joiret, V. Vivier, V. Charbonnier, H. Guerrouj, J. Zhang, et al., Electrochemical Properties and Dissolution Mechanism of A_2Ni_7 Hydrides (A=Y, Gd, La–Sm), ChemElectroChem. 2 (2015) 1321–1330. doi:10.1002/celc.201500163.
[31] M. Pourbaix, J. van Muylder, N. de Zoubov, Atlas d'équilibres électrochimiques à 25 °C, Centre belge d'étude de la corrosion (Bruxelles), Paris: Gauthier-Villars et Cie, 1963.

[32] K. Spahiu, J. Bruno, A selected thermonynamic database for REE to be used in HLNW performence assessment exercises, MBT Tecnologia Ambiental, Cerdanyola . Spain, 1995.
[33] S.G. Bratsch, Standard electrode potentials and temperature coefficients in water at 298.15K, J Phys Chem Ref Data. 18 (1989) 1–21.